Chapter 5

Giant Exchange Bias in Antiferromagnetic $Pr_2CoFe_{0.5}Mn_{0.5}O_6$: A Structural and Magnetic properties study

5.1. Introduction:

A large number of works are devoted to the materials that possess a wide range of physical properties such as giant magnetodielectric effect, metamagnetic transition, GP, large EB, room temperature magnetic ordering, magnetoresistance effects, etc. The promise for the possible applications in spintronic devices with these properties motivated the various research on magnetic materials. Moreover, AFM spintronic devices have much attention over usual FM devices as they acquire the probability of having high data density storage and high-speed devices [226]. Antiferromagnet is used to accumulate and transfer the data in these devices. The ability to have the potential of high data densities device is possible because of the absence of stray fields in an antiferromagnet, whereas these fields are essential to find out and tune magnetization. Stimulation and detection of these materials might be possible electrically, however delivering the data is still less explored [227]–[229]. The EB effect has the potential to detect and control the magnetization data which is generated due to the AFM coupling with FM. This can be understood by the shift in the FM hysteresis loop from the zero-field point in the preferred direction caused by AFM as a consequence of exchange anisotropy [76]. By SOC torque, the EB effect has been used to illustrate the 180º switching of an AFM [230]. To obtain complete control of this, EB needs to be optimized since usually the shifting in the hysteresis loop is gradually degraded in successive hysteresis loops recognized as the training effect (TE) [81], [105]. Recent studies suggested that two different mechanisms may contribute to this phenomenon where one is the thermally activated depinning of AFM spins and domain microstructure in some polycrystalline systems known as thermal TE [231], [232]. Thermal TE caused the decrease in the EB in between every consecutive loop. Whereas, on the other hand, athermal TE is characterized as the large change in the EB field between the first and second hysteresis loop [233]. A. G. Biternas et al explained the detailed dependence of EB field with

hysteresis loop with stability analysis. They showed that maximum stable spins increase from first to the second hysteresis cycle after that stable spins become constant for the athermal TE and further decreases for thermal TE which is associated to the EB field [233]. The major problem is to obtain the stable EB which can be visualized by smallest degradation in consecutive loops.

To investigate in this regard we have chosen a DP having structure $R_2BB'O_6$ (R= rare earth, B/B'= Transition metals) [1-13]. Although the DP systems have widely been studied, there is a lack of studies on structural correlation with the magnetic properties. Moreover, in the present investigation, we have reported the giant and robust EB. The ordered DP Pr_2NiMnO_6 and PCMO facilitate some exotic magnetic and electronic properties of the DP family on the contrary PCFO is the typical member of the disorder DP family which exhibits wealthy magnetic structure and electronics properties such as SPC, EB, GP, SG and G-type magnetic ground state [18], [121]–[124], [239]. The lattice disorder is the result of the development of interesting phases. Both bulks ordered and disordered samples of DP family PCMO and PCFO respectively are rich in magnetic research as well as in structure and electronics properties [122], [125]. With this background, we have chosen PCFMO and investigated the magnetic properties, detailed Raman spectroscopy, and ab initio calculations (DFT).

Additionally, to investigate the magnetic ground state, NPD and XPS have been studied. Since it will become more prominent in the compound having transition metals due to the presence of the mixed chemical state which eventually plays a very significant role in the physical properties of the system.

5.2. Experimental Details:

The particular compound PCFMO understudy has been synthesized by a standard solid-state reaction method using high purity (>99.99%) oxides Pr_6O_{11}, Co_3O_4, Mn_2O_3, and Fe_2O_3 as starting materials. The precursors were mixed in proper stoichiometric ratio and ground in mortar and pestle before initial heating into the furnace at 950 ^{0}C for 24 hours in the air. The obtained powder was reground and carried to several heating cycles at 1100 ^{0}C. Finally, the obtained powder was pelletized and sintered at 1250 ^{0}C for 48 hours at a slow cooling rate to minimize the ASD. The magnetic measurements were carried out using a SQUID-based Quantum Design-MPMS. The neutron diffraction measurements have been performed by a PD2 neutron powder diffractometer (λ=1.2443 Å) at the Dhruva reactor in Atomic Research Centre, Mumbai, India. The Rietveld refinement of the NPD pattern of PCFMO has been done FuLLPROF suite which confirmed that the sample is crystallized in single-phase orthorhombic with Pnma symmetry. XPS experiments were performed by using a scanning X-ray microprobe system equipped with a monochromatic Aluminum Ka X-ray source (1486.6 eV) and a multi-channel Tron hemispherical electron energy analyzer of PHI 5000 VERSAPROBE II, Physical Electronics system. The survey scans, as well as core-level spectra, were measured at an emission angle of 45^o with a pass energy of 50 eV and 11.75 eV, respectively. The binding energy calibration was done by using C 1s located at 284.6 eV. All the photoemission measurements were performed inside the analysis chamber with an average base vacuum of 8.0×10^{-10} mbar. A charge neutralizer was used in order to compensate for the surface charging of the samples. The total energy resolution, estimated from the width of the Fermi edge taken from a cleaned polycrystalline gold sample, was about 400 meV for the monochromatic Aluminum Ka line with a pass energy of 11.750 eV for the core level. The temperature-dependent Raman measurement of PCFMO was carried out with LABRAM-HR800 using the He-Ne laser of the

wavelength of 632.8 nm within the temperature range of 80-300 K in the UGC-DAE Consortium for Scientific Research, Indore, India.

5.3. Results and discussions:

5.3.1. X-ray Photoemission Spectroscopy:

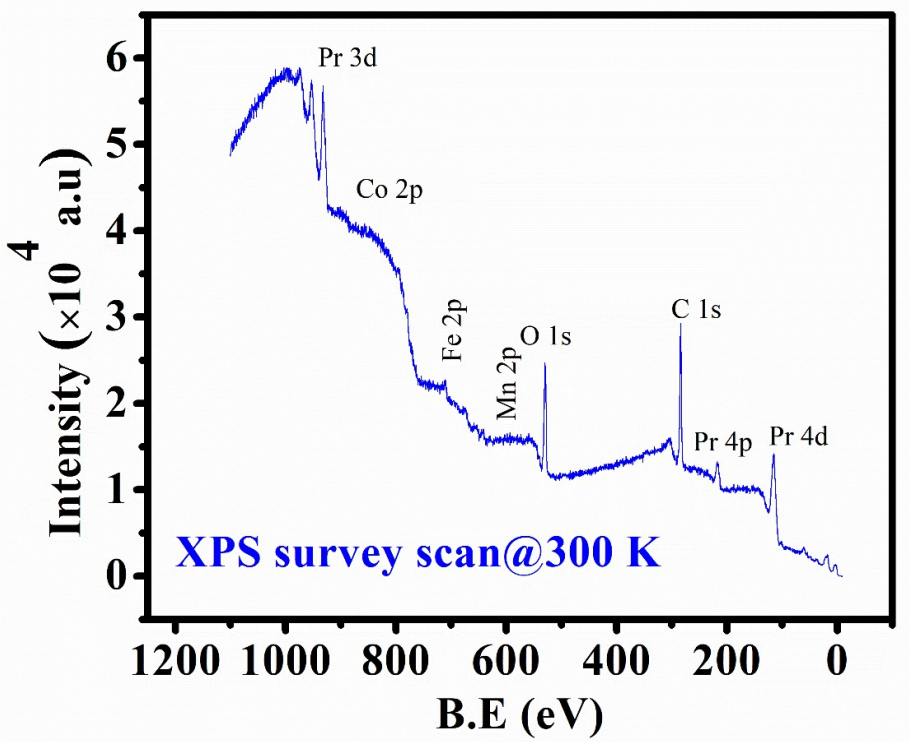

Fig. 5.1: XPS survey scan of PCFMO sample at 300 K.

Fig. 5.1 depicts the survey scan of the PCFMO system which proves the presence of Pr, Fe, Mn, Co, and O in the system. Whereas, no trace of any impurity is detected other than C1s which were incorporated in the sample by the absorption at the surface from the air since C is an adventitious molecule. NIST XPS database has been employed for assigning all the peak positions and doublet separations of the obtained data [240]. Fig. 5.2(a) represents the core level 3d region of Pr which consists of mainly two peaks corresponding to the SOC

peak of Pr $3d_{5/2}$ and Pr $3d_{3/2}$. The Pr $3d_{5/2}$ and Pr $3d_{3/2}$ are located at 933 eV and 953.42 eV, respectively along with the DS of 20.42 eV. Two prominent shoulders-like features at energies just below the main peak are clearly visible and are seemingly associated with the satellite peak. The peak positions and the DS are suggesting the +3 valency of Pr ions [121]. The peak fitting of the core level spectra of Co, Fe, and Mn has been performed with the combination of Lorentzian and Gaussian distribution functions by the XPS Peak fit program. The XPS study of the Co ions is relatively important since its spectra contain satellite peaks that originated from the poorly screened states along with the main peak which is associated with the well-screened states, and these peaks are highly sensitive to the valence state of Co ions. Thus, we have analyzed the Co 2p core-level spectra which are illustrated in Fig. 5.2(b). The spectrum mainly comprises two peaks Co $2p_{3/2}$ and Co $2p_{1/2}$ situated at 794.93 eV and 779.73 eV which are ascribed to the spin-orbit coupling peaks. Whereas, the two broad peaks above the main peaks are associated with the charge satellite peaks. It is pertinent to mention here, that the occurrence of the intense charge satellite peak above the main peaks of Co2p is considered a hallmark of the presence of Co^{2+} ions in the system (typically present in CoO) [176]. In contrast, for Co^{3+} ions, satellite peaks are absent or merely present in the system. However, the Co2p XPS spectrum of Co_3O_4 reveals smaller satellites attribute to the existence of mixed Co^{2+}/Co^{3+} oxidation states [176], [241]. Hence the presence of satellite peaks and the asymmetry and broadening in the peaks is the signature of multiple peaks which is associated with the mixed-valence state of the present cations. Moreover, the DS between $Co2p_{1/2}$ and $Co2p_{3/2}$ is reported to be 15.9 eV for CoO while it comes out to be 15.3 eV for Co_2O_3 [121], [207]. In our system, the obtained DS is 15.5 eV which suggests the presence of more than one chemical state of Co cations. To further elucidate the above observation, we have deconvoluted the Co 2p spectra which again supported the presence of Co^{2+}/Co^{3+} in the system. However, mostly

Co cations are present in the +3 state while there is some finite percentage of +2 states in the system.

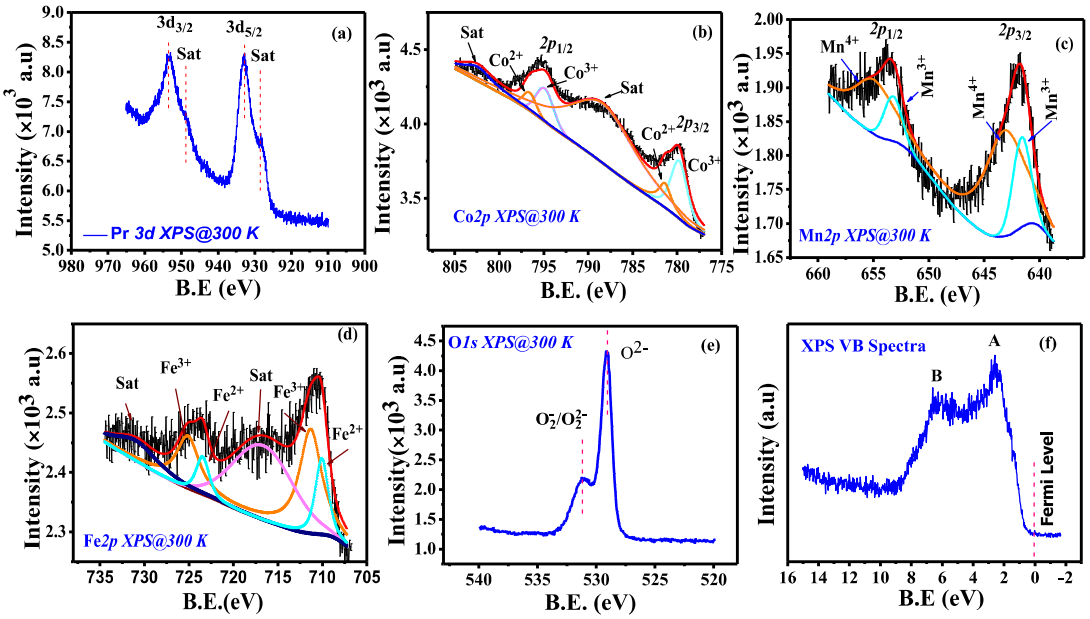

Fig. 5.2 (a) XPS spectra of core level Pr 3d, (b), (c), (d), and (e) illustrate the core level XPS spectra of Co 2p, Fe 2p, Mn 2p, and O 1s, respectively, (f) XPS VB spectra of PCFMO.

We have also analyzed the Mn 2p spectra which contain two peaks Mn $2p_{1/2}$ and Mn $2p_{3/2}$ spin-orbit coupling peaks located at 653.5 eV and 641.77 eV (Fig. 5.2(c)). The peak position of $Mn2p_{3/2}$ is reported at 641.3 eV and 642.2 eV in Mn_2O_3 and MnO, respectively [242]. The intermediate value in our system suggests the mixed-valence state of Mn cations while the DS in Mn2p XPS spectra for MnO_2 is around ~11.8 eV [240]. The reduced value of DS~11.6 eV for PCFMO suggests that the oxidation state of Mn is slightly smaller than +4, which is seemingly associated with the occurrence of fractional Mn^{3+} ions. The analysis by deconvolution also supports the presence of the mixed-valence state of Mn ions in the present system.

Similarly, we have also analyzed the XPS spectra of Fe 2p demonstrated in Fig. 5.2(d). The spectra comprise spin-orbit coupling peaks Fe $2p_{1/2}$ and Fe $2p_{3/2}$ positioned at 723.73 eV and 710.48 eV with DS 13.21 eV. The two broad peaks at ~6.8 eV, above the main peaks, corresponds to the shakeup satellite peaks. The Fe ions of different valence states (e.g., Fe^{2+} and Fe^{3+}) raise the satellite peaks at different positions due to the different electronic configurations (d^6 and d^5). In the XPS spectra of Fe 2p for Fe^{2+} ions, the satellite peak appears at 6 eV whereas for Fe^{3+} the satellite peak appears at 8 eV which can be treated as a hallmark for the different valence states [243]. Hence, the position of satellite peaks suggests the presence of both valence states (Fe^{3+}/Fe^{2+}) in the system. Further, the deconvolution of Fe 2p XPS spectra also yielded the mixed-valence state of Fe ions. Thus, all the above analysis suggests the mixed oxidation of B/B' transition elements in the PCFMO bulk sample.

The spectrum of O 1s has been illustrated in Fig. 5.2(e) which comprised one sharp peak at ~529.1 eV and a weak feature peak at~531.1eV. The peak at ~529 eV ascribed the characteristic feature peak of lattice oxygen "O^{2-}". Whereas, the peak at ~531 eV is known as oxygen species that consists less electrons due to the adsorption of oxygen which leads to the formation of reduced oxygen-rich species (i.e., O_2^{2-} , O_2^- or O^-) [244].

The XPS spectrum near the VB has also been recorded at room temperature to further get insight into the electronic structure of the PCFMO system (Fig. 5.2(f)). The weak spectral weight near the Fermi level indicates the insulating nature of PCFMO. However, the spectrum is mainly composed of the most intense features around ~ 2.5 eV marked as A followed by another feature marked as B around ~6.3 eV. The VB is primarily composed of O2p, Mn3d, Co3d, Fe3d, and Pr4f orbital. Feature A is mainly associated with the hybridization of O2p states with Mn3d, Co3d, Fe3d, and Pr4f orbital in which a prominent contribution comes from Pr4f states. However, feature B is ascribed mainly to the

hybridization of Mn3d/Co3d/Fe3d with O2p orbital. The features (0-1.5 eV) can be attributed to the extended Mn3d/Co3d/Fe3d orbital.

Thus, XPS analysis probes essential information of our system such as the chemical valence state of each constituting element which is important for understanding different exchange interactions in the system. All the B-site elements (Co, Fe, Mn) contain more than one oxidation state (Co^{2+}/Co^{3+}, $Mn^{3+}/Mn^{4+,}$ and Fe^{2+}/Fe^{3+}) in the present system. Moreover, the survey scan attributed no sign of any impurity element in the system, and the VB demonstrated the insulting nature of PCFMO.

5.3.2. Magnetization Study:

Fig. 5.3(a) illustrates the M-T curve with the conventional FC and ZFC protocols where the system has been cooled from room temperature to 2 K. Fig. 5.3(a) is showing a clear transition below a certain temperature (T_c). The large bifurcation between ZFC-FC is attributed to the magnetic anisotropy along with the presence of magnetic spin frustration in the present system. Whereas the ZFC curve shows the negative value of magnetization which can be attributed due to the presence of FM and AFM matrix. The negative magnetization can arise due to the presence of the sublattices which have different temperatures depending on individual sublattice magnetization and the total magnetization is a sum of the magnetizations of each sublattice [245]. In the present system, a disordered statistically distributed mixture of Co, Fe, and Mn cations is present (the disordered Pnma phase was confirmed by the NPD analysis discussed in the NPD section). Further, the magnetization reversal can be attributed to a spin-arrangement according to the G-type canting AFM magnetic structure of the PCFMO system. However, a similar observation of negative magnetization due to the different temperature dependence of individual sublattice for canted AFM G-type system is observed in several reports [245]–[247]. Although, there are several reports on the negative magnetization in the polycrystalline $La_{1-x}Ca_xCoO_3$,

$CaMn_{0.96}V_{0.04}O_3$, $CaMn_{1-x}Fe_xO_3$, and $CaMn_{1-x}Sb_xO_3$ compounds in which antiparallel ordering of the canted moments arising from the $Mn^{3+}(Co^{3+})$-O^{2-}-$Mn^{3+}(Co^{3+})$ and $Mn^{3+}(Co^{3+})$-O^{2-}-$Mn^{4+}(Co^{4+})$ exchange pathways [245], [246], [248]. Despite this, the role of any small trapped magnetic fields in the superconducting magnet during the 'ZFC' cooling can play a crucial in deciding the sign of the magnetization in which the FC and ZFC magnetization curves are a replica of each other [249].

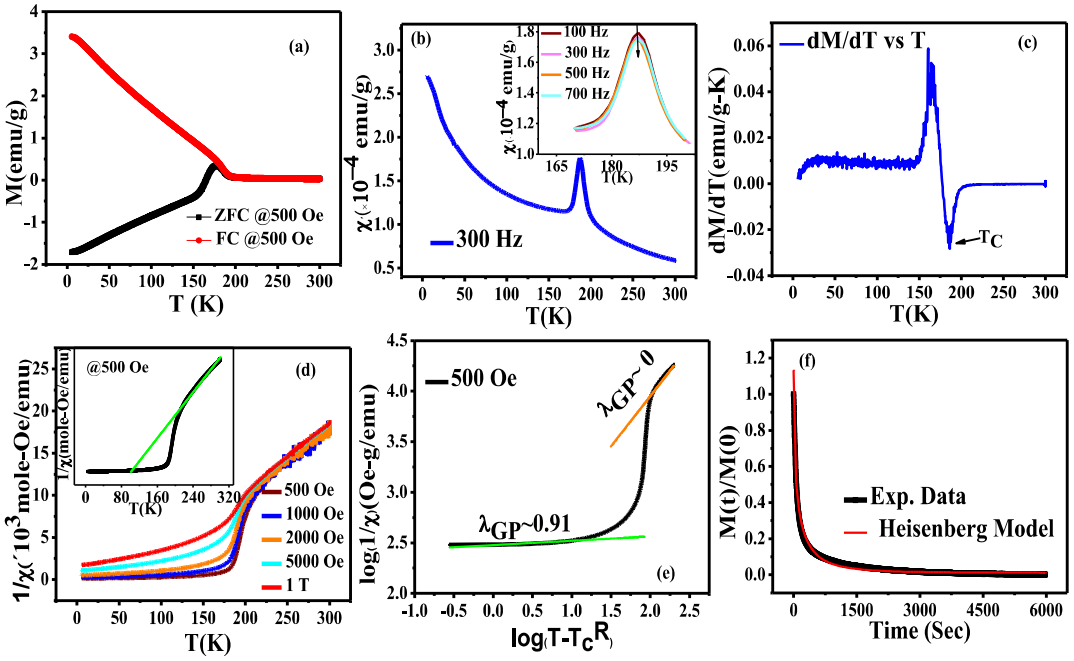

Fig. 5.3 (a) M(T) (ZFC-FC) curve at 500 Oe for PCFMO. (b) Ac χ'(T) curves at 300 Hz while its inset depicts χ'(T) different frequencies, (c) depicts the "dM/dT vs. T" plot. (d) Illustrates the inverse susceptibility vs. temperature curves at different fields while its inset shows a clear deviation from C-W fit at 500 Oe. (e) Shows the power-law fitting to the log-log plot of "$1/\chi$ vs. $((T-T_C^R)/T_C^R)$" (f) Depicts IRM study with its Heisenberg model fitting at 195 K.

To further elucidate the nature of the transition, we have measured the ac susceptibility shown in Fig. 5.3(b). The χ' shows a sharp peak near 186 K confirming the transition temperature of the onset of magnetic ordering of the PCFMO system. The χ' near this temperature range depicts the frequency-independent peak which again evidently suggests

the long-range magnetic ordering near this temperature shown in the inset of Fig. 5.3(b). Furthermore, to precisely identify the nature of the magnetic transition, we have plotted the temperature variation of the dM/dT curve (Fig. 5.3(c)), where M is the ZFC magnetization at 500 Oe applied field. The inflection point of the curve indicates the long-range magnetic ordering transition is at 185 K. To further get insight into the magnetic properties of the system we have plotted the temperature variation of the inverse dc susceptibility at the different fields as demonstrated in Fig. 5.3(d). Interestingly, we have observed the downturn behavior in the temperature variation of the $1/\chi$ curve i.e., the deviation from the CW law occurs since the magnetization does not follow the analytic function of magnetic fields (inset of Fig. 5.3(d)). The downturn behavior in $1/\chi$ commences well above the transition temperature and starts to diminish as the applied magnetic field increases and attains CW-like behavior which is a signature of GP. The $1/\chi$ follows the power law (modified CW law) in the GP regime at low fields [73], [74];

$$\chi^{-1}(T) \propto (T-T_c^R)^{1-\lambda}, (0<\lambda<1) \quad 5.1$$

Where λ is the characteristic non-universal exponent which measures the deviation from the CW law thus describing the GP singularity and T_c^R is the critical temperature of random FM. The value of T_c^R is chosen such that it efficiently yields $\lambda \sim 0$ in the PM region. A reasonable choice for T_c^R is Curie temperature which has been obtained by CW fit in the PM region. The yielded value of λ is 0.91 confirming the existence of GP in the system (Fig. 5.3(e)). To further elucidate the presence of the additional magnetic cluster in the PM matrix, we have also utilized the spin relaxation measurement by performing the TRM measurement above T_C. In our case, the magnetization relaxation decay appears to behave by the Heisenberg model as illustrated in Fig. 5.3(f). The nature of the spin correlation is inferred that the spin relaxes slowly due to the clusters in the PM region, thus establishing the presence of the GP in the PCFMO system. The ASD has been enhanced at B-site on the

doping of 50% Fe at Mn-site by creating further frustration due to the mixed-valence state. In addition to the mixed oxidation state, the arbitrary distribution of Co/Mn/Fe ions generates different competing interactions that are the key ingredient of the nucleation of FM clusters. Interestingly, both the end members of the PCFMO system (PCMO and PCFO systems) showed the GP [124], [125].

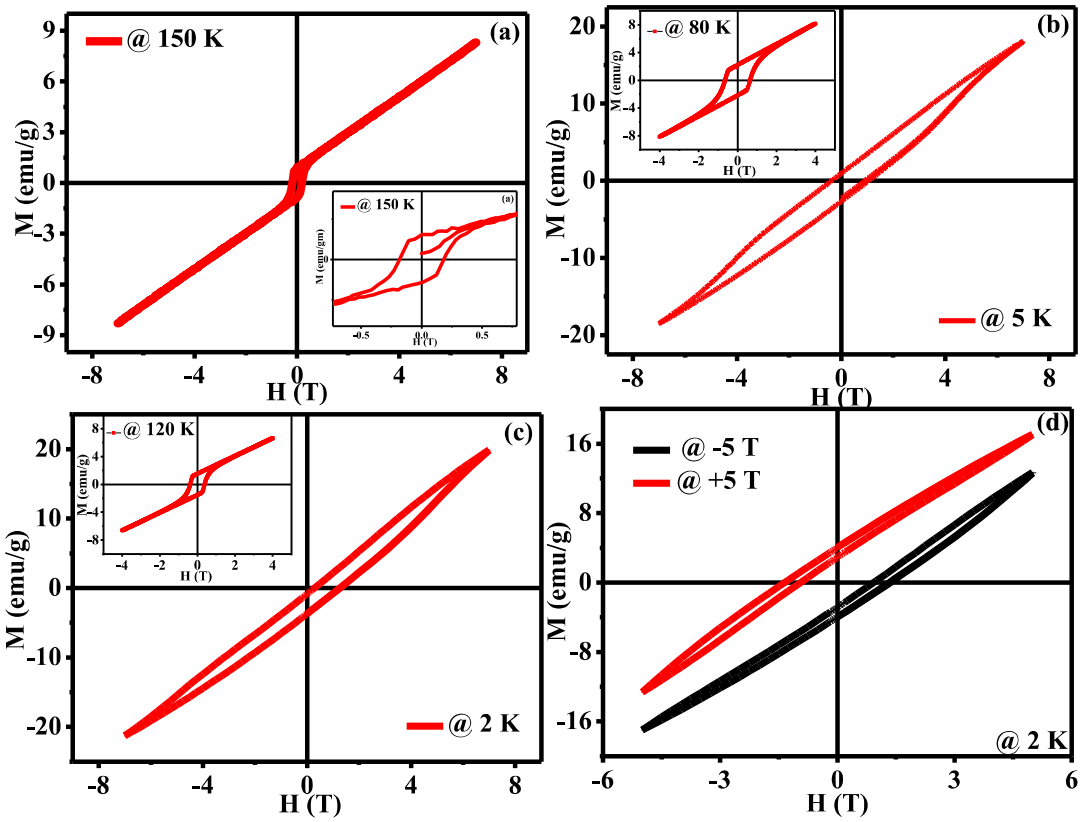

Fig. 5.4: (a) M(H) curves at 150 K while its inset shows the close-up view of the hysteresis curve. (b) and (c) show M(H) curves collected at 2 K and 5 K in ZFC mode, respectively while their inset show M(H) curves at 80 K and 120 K, respectively. (d) M(H) curve measured at 2 K in FC mode with ± 5 T.

To further explore the magnetic nature of the present system we have recorded the M(H) loop at different temperatures. The M(H) loop recorded at 150 K (below the transition temperature) with Hc= 1834 Oe is illustrated in Fig. 5.4(a). The inset of Fig. 5.4(a) discerns

hysteresis nature with the large coercive field which is the manifestation of common FM or FIM materials as a result of the blocking of domain wall motion. On the other hand, magnetic moment saturation has not been achieved up to such a high applied field of 7 T is a characteristic of the presence of large AFM interaction along with FM interaction in the system. Whereas M(H) curve at 80 K and 120 K shows similar behavior as the 150 K hysteresis curve, the only noticeable difference is the increase in the coercivity as we move from high to low temperature (150 K to 80 K) (inset of Fig. 5.4(b) and 5.4(c)). However, the one end member of the present system is PCFO which is a canted AFM system due to the superexchange interactions via $Co^{3+}/Fe^{3}+$ ions whereas another end member, PCMO is FM (via 180º superexchange interaction Co^{2+}-O^{2-}-Mn^{4+}) along with some disorder due to the occurrence of Co^{3+}/Mn^{3+} ions [18], [124]. As the XPS study indicates, the presence of different ions (Co^{2+}, Co^{3+}, Fe^{3+}, Fe^{2+}, $Mn^{3+,}$ and Mn^{4+}) produced multiple competing AFM/FM interactions in the system. The difference in charge states at B/B' sites (i.e., B^{2+}-O^{2-}-B'^{4+} where B=Co/Fe and B'=Mn) is generated by FM interaction in nature which can be best understood by the 180º superexchange interaction according to the Goodenough-Kanamori rule while the same charge states create (B^{2+}-O^{2-}-B'^{2+}/B^{2+}-O^{2-}-B^{2+}, B^{3+}-O^{2-}-B'^{3+}/B^{3+}-O^{2-}-B^{3+} and B^{4+}-O^{2-}-B'^{4+}/ B^{4+}-O^{2-}-B^{4+}) AFM interaction in the system. Hence, dominating AFM interaction along with the FM interaction is the manifestation of the presence of different ions in the present system. Thus, the competition between FM/AFM interaction as discussed by XPS and M(T) data is again well supported by the MH loop at 150 K. As a matter of fact, the intriguing phenomenon with horizontal or vertical displacement in the M(H) curve known as the EB effect can arise as a result of the different exchange interactions at the interface between FM and AFM components [76], [112]–[114]. Since PCFMO hosts multiple magnetic phases thus it is a potential candidate for arising EB effect in the system. To elucidate the existence of the EB effect, we have

performed the EB measurements with two standard protocols: (i) the M(H) loop has been recorded in ZFC mode by cooling the sample from room temperature to the desired temperature in the absence of dc bias field mode known as SEB whereas in the (ii) M(H) loop has been recorded in FC mode by cooling the sample from room temperature to the desired temperature in presence of applied field famously known as CEB [239]. Fig. 5.4(b) demonstrates the MH loop at 5 K in ZFC mode which is highly asymmetric as the hysteresis loop moves entirely to the left side providing clear evidence of the EB effect. The quantitative analysis of EB can be done by estimating the EB field as $H_E=|H_{C1}+H_{C2}|/2$, and coercivity as $H_C=|H_{C1}-H_{C2}|/2$ where H_{C1} and H_{C2} are denoting the left and right coercive field values of M(H) loop. The obtained values of H_E^{SEB} and H_C^{SEB} for PCFMO are ~0.3222 T and ~0.6571 T respectively. Similarly, other EB characteristics can be defined as remanence asymmetry $(M_E)=|M_{R1}+M_{R2}|/2$ and magnetic coercivity $(M_C) =|M_{R1}-M_{R2}|/2$, where M_{R1} and M_{R2} are the remanent magnetization values at H=0 field. The observed values of M_E and M_C are found to be ~0.8792 emu/g and ~1.8443 emu/g respectively. The Fig. 5.4(c) displays the M(H) loop at 2 K in ZFC mode which clearly indicate the presence of SEB as the entire loop shifted towards the right side. Interestingly, the observed values of H_E^{SEB} and H_C^{SEB} at 2 K are ~0.7736 T and ~0.4903 T respectively which is significantly large, whereas M_E^{SEB} is nearly 2.2848 emu/g and M_C^{SEB} is nearly 1.4079 emu/g. It is pertinent to mention here that SEB effect is not in measurable scale for both the end members (PCMO and PCFO) of the present system. Thus, for PCFMO an entire loop shift has been observed even in the zero applied dc field is particularly striking. On the other hand, for investigating the CEB, we have also performed the aforementioned measurement of CEB at 2 K with the ±5 T applied dc field. As illustrated in the Fig. 5.4(d), the M(H) loop is entirely shifted to the left side for the applied field of +5 T (P-type) whereas the loop is symmetrically opposite and shifted towards the right side for -5 T (N-type) field which suggest that the

obtained CEB is not generated from the non-saturated minor loop. The obtained values of H_E^{CEB} and H_C^{CEB} are ~1.15 T and ~0.2076 T respectively. Similarly, the CEB showed the value of M_E^{CEB}~3.94 emu/g and M_C^{CEB}~2.85 emu/g. Thus the observation of such giant value of loop shift (~1.15 T) for our system is comparable to the other observed giant EB systems[113], [250], [251].

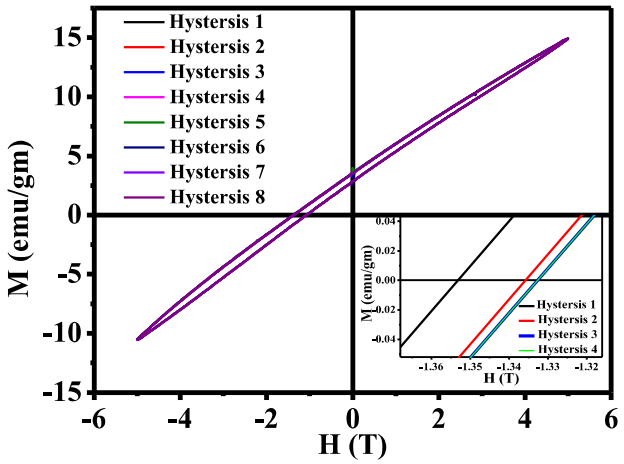

Fig. 5.5 Training effect at 2 K in CEB mode while its inset shows a closer view of the degradation in the loops only up to 4th loop.

In addition, one more important aspect to measure an EB system is TE. During this process, the uncompensated spins at FM/AFM interface are aligned in the direction of the applied field thus the stability of the EB can be probed by TE [252], [253]. The TE is realized as the change in the H_E and symmetry between the first to the consecutive number of loops [252]. Most intriguing, in Fig. 5.5 second and subsequent loops seem to overlap on the first hysteresis loop, only the enlarged view represents a small shift in the hysteresis loop (inset of Fig. 5.5). The H_E values show a negligibly small change from 11500 Oe to 11384 Oe (~1%) for tracing the hysteresis loop from n=1 to n=3. Such an insignificantly small decrease in the EB field as compared to the obtained giant H_E establishes the presence of

stable EB and lack of training in the system. Similar results have been recently reported by Sarah Jenkins et. al. [254]. They have identified the cause of such reduction in EB field by atomistic model and then proposed that training is an interface effect that can be optimized by the flat interface. Similarly, the lack of TE and stable EB has occurred for the non-dilution where the AFM interface is completely compensated with all the spins which stabilize individually the number of hysteresis loop cycles. There can be the largest EB field with the smallest TE for the finest value of dilution [234]. Experimentally, Minghu Pan et al. showed that the only parameter which affects the thermal stability of the EB field is AFM layer thickness [255]. Since the different thickness of the AFM layer has a different distribution of grain size it achieved different blocking temperatures [255]. Thus, such a remarkably small TE is advantageous for wide applications.

Thus, as a result of the aforementioned discussion on the magnetic properties of the PCFMO system, we can identify the occurrence of the GP, SEB, and CEB in the present system. GP and EB phenomena have been established by conducting different measurements and analyses such as inverse dc susceptibility, modified CW, relaxation measurement, and P-type and n-type EB effects. The most appealing feature of the present system is the presence of a nearly absent TE. These interesting phenomena are the consequence of the presence of both FM and AFM interaction.

5.3.3. Neutron diffraction study:

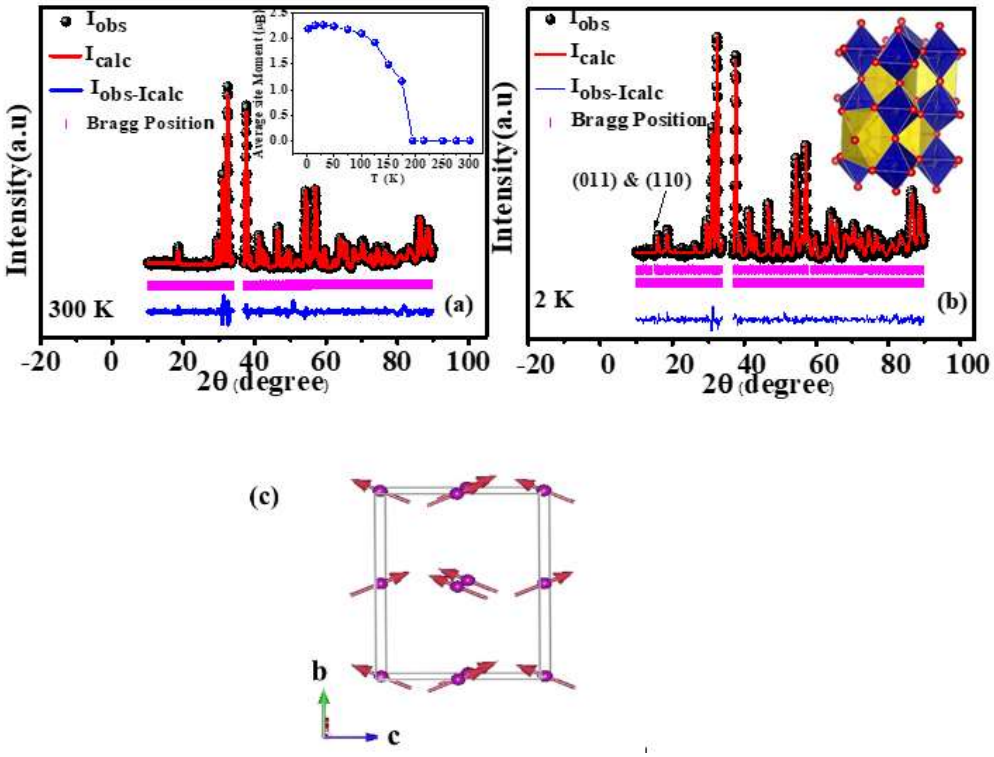

Fig. 5.6: (a) and (b) The NPD pattern along with its Rietveld refinement at 300 K and 2 K, respectively while their inset shows the thermal variation of average site moment and Octahedral Crystal structure of PCFMO with space group Pnma, respectively. (c) G-type canted AFM structure generated by NPD at 2 K.

To obtain insight into microscopic spin arrangement as well as the crystal structure and the structural order in the PCFMO system, we have performed NPD at different temperatures. In order to ascertain the crystal structure and degree of ordering of Co, Fe, and Mn ions, NPD at room temperature along with its Reitveld refinement is illustrated in Fig. 5.6(a). Usually, the ordered DP crystalline in monoclinic structure with $P2_1/n$ space group, where Co occupies in 2c Wyckoff position, however, Fe and Mn occupy the 2d Wyckoff position in our system. On the other hand, if the cations are randomly disturbed or crystalline in a disordered structure then it can be described by orthorhombic structure with Pnma space group where Co, Fe, and Mn all cations occupy the common 4b Wyckoff position. The

difference in the scattering length of Co (2.49 fm), Fe (9.45 fm), and Mn (-3.75 fm) for neutron allows us to probe the exact crystal structure of the PCFMO system. Our first attempt was to refine our sample with B-site cation ordered monoclinic structure and $P2_1/n$ space group at 300 K. Whereas, for the cations ordered structure, (011) peak appears in the diffraction pattern [168]. The absence of this peak at 300 K eliminates the presence of a B-site ordered structure in the PCFMO system. Moreover, as our XPS analysis reveals the presence of a large percentage of Fe, Mn, and Co ions are in a +3 state however for a monoclinic structure with $P2_1/n$ symmetry minimum charge difference needs to be +2 between B-site cations. Thus, the system is crystalline in the orthorhombic phase with the Pnma spacegroup. The refined atomic positions, lattice parameters, bond angles, and bond lengths at 300 K and 2 K are tabulated in table 5.1. The absence of any magnetic reflection contribution to the fundamental crystal structure reflections at room temperature in NPD supports the transition temperature below 300 K. Further temperature-dependent NPD analysis yielded the appearance of a super-lattice reflection below 185 K and gains the maximum intensity at 2 K as shown in Fig. 5.6(b). NDP below 185 K illustrates two reflections (110) and (011) at $2\Theta \sim 16°$ that cannot be resolved well within the resolution limit of the diffractometer. The nuclear contribution to the appeared reflection (011) is nearly absent or minimal in the Pnma phase. The obvious magnetic contribution in the reflections (110) and (011) have appeared in the P-1 (magnetic phase) space group and does not associate with any structural change. The gradual increase in the intensity of (110) and (011) at $2\Theta \sim 16°$ peak with lowering of temperature is demonstrated in Fig. 5.7.

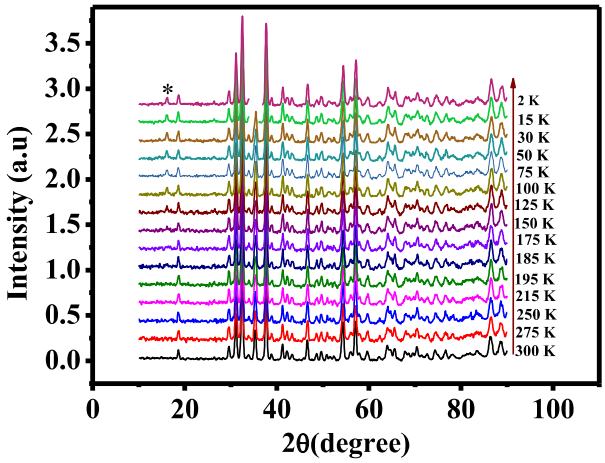

Fig. 5.7: NPD pattern at different temperatures.

The yielded microscopic spin alignment for PCFMO at 2 K is shown in the schematic diagram in Fig. 5.6(c). The irreducible representation is yielded using BasIreps with the propagation vector k = (0, 0, 0). The obtained spin ordering by NPD pattern analysis is a canted AFM type magnetic structure where this spin arrangement is GzFy type. The AFM G-type magnetic ordering is directed along the z-direction whereas the FM moment is aligned in the y-direction according to this structure. Thus, this spin arrangement leads to the dominating AFM interaction in the system. Although, due to the presence of spin canting FM behavior should also reside in the system along with the dominating AFM background. It is relevant to mention here that the spin arrangement is similar to the PCFO system [18]. Thus, the neutron analysis is well consistent with the magnetization results. The temperature variation of the average site moment is shown in the inset of Fig. 5.6(a) in which the maximum moment of Fe/Co/Mn is 2.194 μB per site at 2 K. No change in the crystal structure and the magnetic structure has been observed till 2 K with the magnetic moment 2.194 μB whereas the average saturation moment of Co^{3+} (4μB in the HS state), for Fe^{3+} (5μB in the HS state) and Mn^{3+} (4μB in HS). However, the saturation spin-only moment for Mn^{4+}, Co^{2+} and Fe^{4+} are 3μB, 3μB, and 4μB considering each element in the

HS state supports that our system contains the finite percentage of these valences along with Co^{3+}, $Fe^{3+,}$ and Mn^{3+} as suggested by XPS analysis. As a matter of fact, further reduction at the moment indicates the presence of ASD in the system. Hence, the NPD gives an insight of the crystal structure, magnetic spin structure as well as the ASD of the present system. The system retains the orthorhombic phase with Pnma spacegroup throughout the temperature. Moreover, the magnetic superlattice peak that emerges in the spectra just below 187 K indicated the LRO below this temperature which supports the magnetization data. The yielded ground state spin structure is canted G-type AFM leading to the quite small value of obtained maximum site moment as compared to the fully saturated moment of the constituting cations. Thus, the system as the ground state is canted AFM structure, we cannot rule out the possibility of competing FM/AFM interaction. Thus, there are FM and AFM components in the system in different crystallographic directions as the system as the ground state is canted AFM structure. However, the above discussion suggests that in the present system there could be some regions are enriched in Co^{2+} or Mn^{4+} ions and generating FM sublattice via Co^{2+}—O^{2-}—Co^{2+}/ Mn^{4+}—O^{2-}—Mn^{4+} and others have strong AFM interactions due to the presence of Co^{3+}/Fe^{3+}/Mn^{3+} oxidation states. Hence, PCFMO is a complex system that may have both the competition between FM/AFM interaction and FM/AFM sublattice in the system.

Table 5.1: Structural parameters obtained from the Rietveld profile refinement of the NPD for PCFMO at 300 K and 2 K with Space group: Pnma.

NPD recorded at	300 K	2 K
Pr	4c	4c
x	0.0382(6)	0.04081
y	0.25000	0.25000
z	-0.0060(13)	-0.01077
B_{iso} (Å^2)	0.62(5)	0.39952
Co	4b	4b
x	0.00000	0.00000
y	0.00000	0.00000
z	0.50000	0.50000
B_{iso} (Å^2)	0.28(7)	0.16739
Fe	4b	4b
x	0.00000	0.00000
y	0.00000	0.00000
z	0.50000	0.50000
B_{iso} (Å^2)	0.28(7)	0.16739
Mn	4b	4b
x	0.00000	0.00000
y	0.00000	0.00000
z	0.50000	0.00000
B_{iso} (Å^2)	0.80744	0.16739
O(1)	4c	4c
x	0.4877(7)	0.48449
y	0.25000	0.25000
z	0.0769(8)	0.07580
B_{iso} (Å^2)	0.67(5)	0.58744
O(2)	8d	8d
x	0.2873(5)	0.28863
y	0.0387(3)	0.04052
z	-0.2887(5)	-0.28679
B_{iso} (Å^2)	0.63(3)	0.41215
$d_{Co-O(1)}$(Å)/$d_{Mn-O(1)}$ (Å)/ $d_{Fe-O(1)}$(Å)	1.9715	1.9659
$d_{Mn-O(2)}$ (Å)/$d_{Co-O(2)}$(Å) $d_{Fe-O(2)}$ (Å)	1.9789	1.9851
<(Mn)-(O1)-(Mn)>(deg)/ <(Co)-(O1)-(Co)>(deg)/ <(Fe)-(O1)-(Co)>(deg)	170.39	170.247
<(Mn)-(O2)-(Mn)>(deg)/ <(Co)-(O2)-(Co)>(deg)/ <(Fe)-(O2)-(Co)>(deg)	171.37	171.128

5.3.4. Ab initio calculations (DFT) of the electronic band structure:

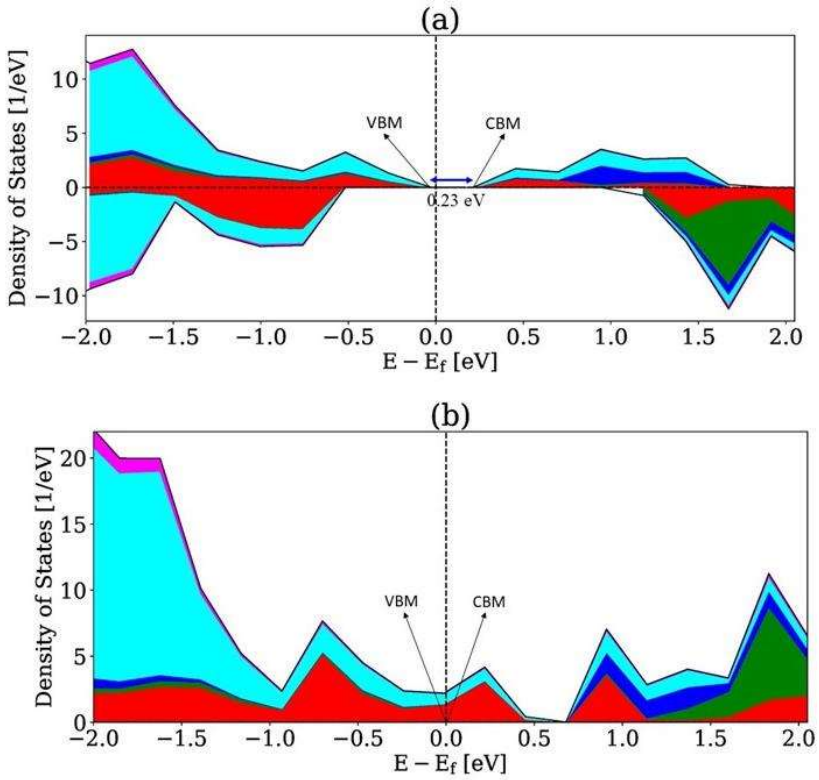

Fig. 5.8: (a) Shows the TDOS and PDOS without SOC obtained from spin-polarized DFT calculation similarly, (b) shows the TDOS and PDOS with SOC from DFT calculation wherein both the figs the black line represents the TDOS, and PDOS of each element is represented by stacking manner for FM configuration, where VBM and CBM are valence band maxima and conduction band minima, respectively.

We employed an *ab initio* numerical calculation of PCFMO using VASP version 6.1.2. The lattice parameters (lattice length and angles) and atomic coordinates are extracted from experimental data in the same work. We used a package SOD 0.47 to generate all the possible doping sites of Mn, and Fe in the Co atomic sites and select one of the doped structures that we think is closest to experiments, which we then run for a VASP calculation [256]. The basis sets we choose for Pr, Mn, Fe, Co, and O is the PAW and a cutoff value was set to 400 eV. The exchange-correlation functional is GGA-PBE. We relaxed the cell shape, cell volume, and atomic position while preserving its space group symmetry Pnma.

To include the electron correlation interaction in this material, we used Hubbard U values of 6.0, 5.3, 3.9, and 3.8 eV for Pr, Fe, Mn, and Co respectively. After we converged the structure and electronic configurations, we analyzed the electronic properties in terms of the TDOS, and also the PDOS, in which the original DOS is decomposed into each element' DOS. We showed PDOS results in Fig. 5.8.

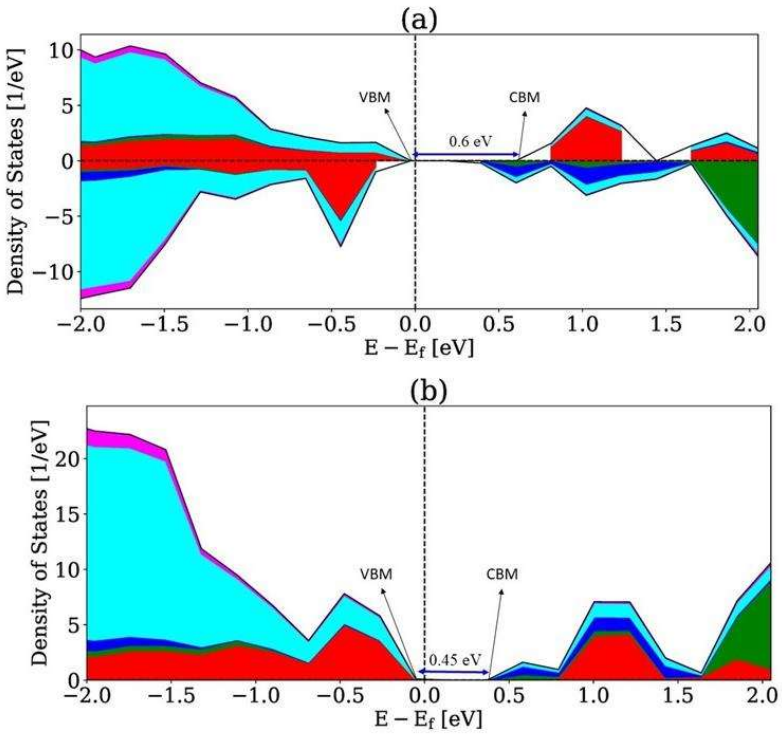

Fig. 5.9: (a) The TDOS and PDOS are depicted for the 'without SOC' and AFM spin configuration. It shows FM state is energetically more stable. In contrast, (b) shows the TDOS and PDOS after considering the 'SOC' effect in the calculations for the AFM spin configuration. In this case, AFM shows a more favourable state than FM.

From Fig. 5.8(a), we found a small gap of 0.2 eV appears near the Fermi level for the spin-up channel, and a much larger gap of 2 eV emerges for the spin-down channel. The SOC results, nevertheless, suggest that the sample can become conducted from Fig. 5.8(b). From the PDOS, we found that the DOS near the Fermi level was dominated by Co, and O, and the contribution of the rest atoms to the DOS near the Fermi level was negligible. In

parallel, we performed a similar calculation assuming an AFM configuration (Fig. 5.9). The spin-up channel has shown a bandgap of 0.8 eV, and also the spin-down channel has a slightly smaller gap but remains insulating (Fig. 5.9(a)). After we apply SOC, the results persist as an insulator with a bandgap of 0.3 eV (Fig. 5.9(b)). The DOS near the Fermi level is dominated by Co, Mn, Fe, and O, where Pr atoms contribute nearly zero electronic states. Following Table 5.2, without including SOC, FM is 0.17 eV more stable than AFM, whereas after considering SOC, the energies were reversed, predicting AFM becomes 0.33 eV lower than FM. From the DOS just shown, we also found AFM predicts a bandgap for with and without SOC, whereas for FM, only without SOC, we found a bandgap, and for with SOC case, the bandgap disappears and becomes conducting. Comparing these with experimental data, we observe that the AFM results are more reliable from the perspective of bandgaps and the lower total energies obtained. This suggests that the insulating nature of our system is induced by the Coulomb-assisted SOC as similarly observed in some other DPs systems [201], [257]. Thus, the electronic structure obtained by the ab intio calculations is well consistent with experimental results indicating the AFM ground state with the insulating nature of the system.

Table 5.2: The total energy of PCFMO using different spin configurations without SOC and with SOC considerations.

Spin configuration	**Energy (eV)**
FM without SOC	-148.671112
FM with SOC	-149.221915
AFM without SOC	-148.500791
AFM with SOC	-149.557848

5.3.5. Temperature-dependent Raman Study:

It is well accepted that the Raman scattering can be employed as a probe for a sensitive change in the local structure due to the presence of disorder, SPC, electron-phonon

coupling, etc [97], [123], [159], [258]. The chemical substitution at A and B-site with different ionic radii caused the distorted perovskites via co-operative rotation or tilting of octahedral, B-site ordering, and displacements of cation at A and B-site. Structural analysis by NPD patterns reveals that the PCFMO system has been crystallized in the orthorhombic phase in the Pnma space group. Less number of Raman modes are visible in the disordered DPs which emerge in the orthorhombic structures with Pnma space group in which B and B' cations are randomly distributed identically as to ABO_3 systems) [121]. Whereas, additional Raman modes are visible in the monoclinic symmetry because of the increase in the effective lattice parameters via the folding Brillouin zone [161]. While the group theory analysis suggests 60 r-point phonons modes which decompose in 24 ($7A_{1g}+5B_{1g}+7B_{2g}+5B_{3g}$) Raman active modes, 25 infrared active modes, 8 silent modes, and the remaining 3 are acoustic modes for orthorhombic phase (Pnma space group) [217], [259]. Fig. 5.10(a) depicts the room temperature Raman spectra where the most intense mode is observed at 628 cm^{-1} and a broad peak is situated at 518 cm^{-1}. Schematically, the modes that lie below 200 cm^{-1} are associated with the displacement of rare-earth ions while the modes situated above 300 $cm^{-1}$are characterized solely as the motion of light oxygen ions. The vibration modes in the intermediate frequency range belong to both the ions. Thus, the predominant mode at ~630 cm^{-1} and ~518 cm^{-1} is assigned to the symmetry (Ag) and asymmetry/bending stretching (Bg) vibrations of $(Co/Mn/Fe)O_6$ octahedra, respectively. The broadness of the peak (especially 518 cm^{-1} modes) might be associated with the three-transition metal octahedral with an almost similar stretching frequency range. Moreover, the Bg mode shifts to the higher wavenumber region as compared to parent systems suggesting the compressive strain or hardening nature due to the doping of Fe at the Mn site [121].

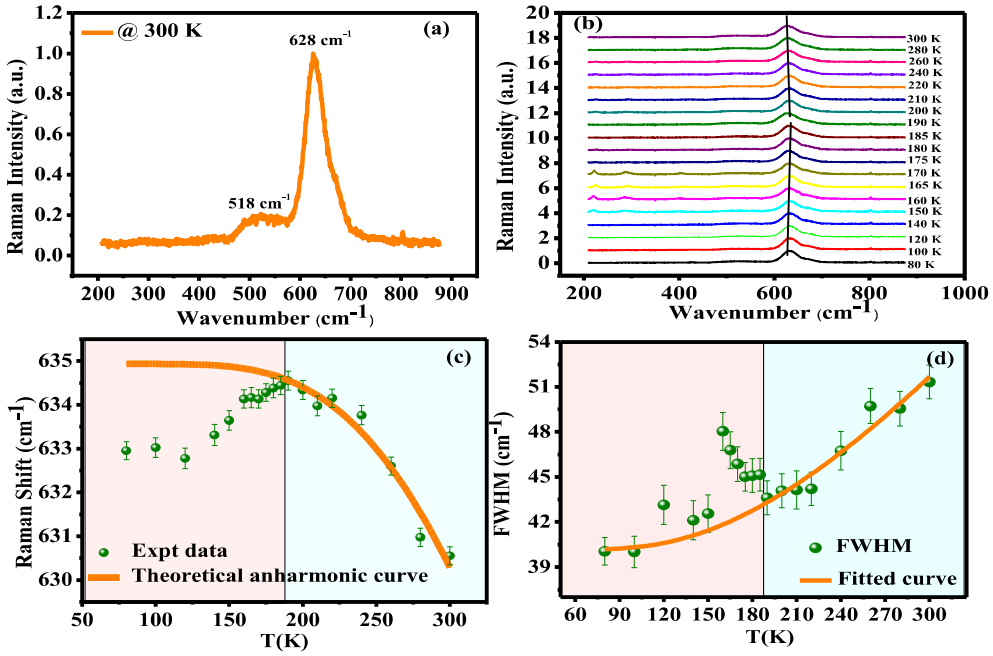

Fig. 5.10 (a) Raman spectra at room temperature. (b) Raman spectra at different temperatures. (c) The anharmonic fit to the temperature-dependent Raman shift of stretching mode. (d) Temperature variation of the FWHM of the stretching mode with the anharmonic fit.

To further elucidate the structural change and the effect of temperature on the magnetic ordering, temperature-dependent Raman spectra have been analyzed and shown in Fig. 5.10(b). The absence of any structural transition in the temperature range of 80-300 K is suggested due to the non-appearance of any additional mode and non-appearances of any remarkable shape change in the system in this temperature range. Moreover, the anomalous behavior in the Ag mode position indicates the presence of SPC across Tc. To further get a clear insight into the effect of temperature on the Ag mode Raman shift is depicted in Fig. 5.10(c). Balkanshi has proposed that the phonon frequency follows the anharmonic behavior in the absence of any structural transition and any coupling between spin and phonon [221]. Thus, according to this model the variation in Raman shift with temperature is ascribed by the following anharmonic relation:

$$\omega_{anh} = \omega_0 - C\left(1 + \frac{2}{e^{\frac{\hbar\omega_0}{K_B T}} - 1}\right) \quad 5.2$$

Where, ω_0 and C are the adjustable parameters, ħ is Planck's constant, and K_B is the Boltzmann constant. Generally, on decreasing the temperature of the system, the phonon excitation frequency gets hardened to a particular temperature after that it attains a plateau at a sufficiently low temperature. Since the present system follows the anharmonic behavior near Tc which suggests the dominating contribution of an anharmonic effect till Tc as illustrated in Fig. 5.10(c). Whereas, phonons do not exhibit the usual behavior proposed by Balkanshi, exhibiting clear deviation from the anharmonic fit below Tc. Thus, the involvement of the magnetic ion vibrations which essentially induced the modulation in the lattice vibration plays an essential role here. Thus, the anomalous softening in the phonon mode near Tc comprehended the presence of SPC [161], [220], [222], [260]. In addition, to ascertain the magnetic ordering effect on phonon frequency the FWHM at different temperatures can be employed as FWHM (or linewidth) is a measure of phonon lifetime which in turn relates differently due to the magnetic transition and due to the change in lattice parameters (magnetostriction effect). Since the dominating scattering mechanisms should be temperature independent from the lattice defects and temperature-dependent for phonons [219], [223]. Thus, FWHM has been plotted with temperature and is illustrated in Fig. 5.10(d). PCFMO clearly shows a sudden increase in the FWHM near magnetic transition which discards the possibility of the coupling due to the magnetostriction effect. The decrease in linewidth (or FWHM broadening) suggests the decrease in phonon lifetime below T_C. Further, purely anharmonic contributions estimated by Balkanski's model are expressed as [221]

$$\Gamma(T) = \Gamma_0\left(1 + \frac{2}{e^{\frac{\hbar\omega_0}{K_B T}} - 1}\right) \quad 5.3$$

Here, Γ_0 is a fitting parameter. According to this, $\Gamma(T)$ should be increased monotonically as the temperature increases at high temperatures and should become constant at low temperatures in the absence of the SPC. Fig. 5.10(d) depicts the clear anomaly near magnetic transition and deviation from the theoretical model points out toward the modulation of phonon lifetime near magnetic transition due to the local lattice instabilities at transition. Thus, such an anomaly across magnetic transition temperatures in the line shape parameters of vibrational phonon mode emphasizes that the phonon anomaly is induced solely due to the SPC. Further, within the mean-field approximation, any magnetic material having LRO promotes the renormalization of phonon frequency due to the SPC [97], [218], [261].

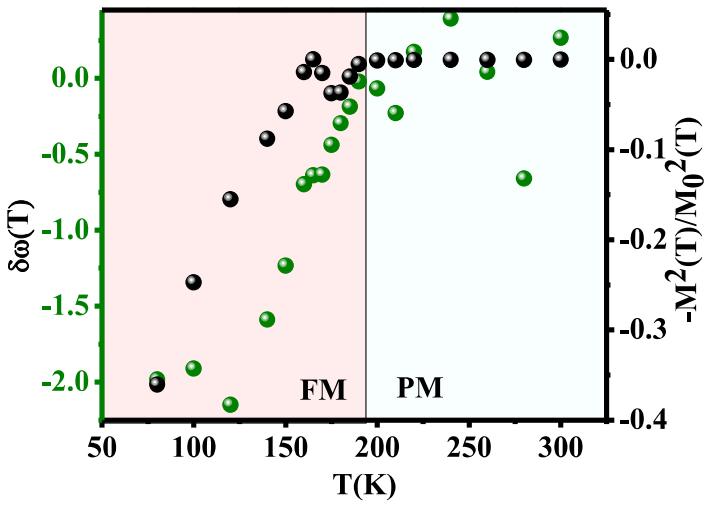

Fig. 5.11 Thermal variation of δω(T) and $\left(\frac{M(T)}{M_0}\right)^2$ of Ag stretching mode.

The renormalized phonon frequency is directly proportional to the spin-spin correlation function <SiSj>for the nearest neighbor spin localized at the i^{th} and j^{th} site. According to this model, the λ<SiSj> can be represented as follows:

$$\delta\omega(T)= \lambda<SiSj> = \left(\frac{M(T)}{M_0}\right)^2 \quad 5.4$$

Where $\left(\frac{M(T)}{M_0}\right)^2$ is the normalized magnetic moment, λ is the phonon coupling constant, and δω(T) is the difference between the theoretical phonon frequency obtained by the anharmonic model and the observed phonon frequency. Fig. 5.11 depicts quite a good overlap between the normalized magnetic moment and the variation in phonon frequency. The two curves follow nearly similar trends as they overlap till Tc and start deviating from the linear nature just below Tc which unambiguously establishes the occurrence of the strong interplay between the microscopic degrees of freedom, highlighting the significance of cooperative effects of microscopic degrees of freedom in such system via SPC. Whereas, the lack of full overlap in both the curves can be presumably ascribed to the mixed-valence state (Co^{2+}/Co^{3+}, $Fe^{3+}/Fe^{4+,}$ and Mn^{3+}/Mn^{4+}) which creates ASD in the system as described by the XPS study. As a result, some additional FM (i.e., Co^{2+}-O-Fe^{4+}, Fe^{3+}-O-$Mn^{3+,}$ Co^{2+}-O-Mn^{4+}, etc) and AFM interactions (Fe^{3+}—O^{2-}—Fe^{3+}, Co^{3+}—$O^{2—}Fe^{3+}$, Mn^{3+}—O^{2-}—Mn^{3+}, Co^{2+}—O^{2-}—Co^{2+}, Mn^{4+}—O^{2-}—Mn^{4}, etc) generates in the system via super-exchange interactions [9], [262]. As a consequence, competition between FM and AFM interaction creates different phases such as AFM and FM in the present system. Different interactions create different exchange interactions and coupling values in the system which play different roles in the SPC. Thus, complexity has been generated in the system due to ASD. Similar behavior due to ASD has been observed in some other systems [196], [219]. Thus, the above discussion emphasized the interplay between the magnetic spin and phonon renormalization in our system.

5.4. Conclusion:

In conclusion, the core level analysis of transition metals confirms more than one chemical valence state of Co, Fe, and Mn ions. Moreover, the VB of XPS reveals the insulating

nature of the system which is well consistent with the theoretical result. Further, the magnetic properties of our system reveal the existence of both AFM/FM interactions in the system. Both the interaction can be easily interpreted by the mixed-valence states which generate complexity in the system. Whereas, both dc (MT and dM/dT) and ac susceptibility studies reveal the long-range magnetic transition temperature at 187 K. The inverse dc susceptibility exhibits the presence of a GP by showing downturn behavior above the magnetic transition. The presence of coexisting phases creates the interface between FM and AFM which provokes a system to show EB phenomena. Both conventional and spontaneous EB effect is present in our system with very large values. Moreover, both the end member PCFO and PCMO only showed CEB which makes our system rich in magnetic properties. TE analysis reveals such stable EB as it decreased less than 1% in the third consecutive loop. Structural analysis of the Pnma space group at room temperature Raman spectra is well consistent with the NPD result. Further, the peak positions of phonon modes deviate from the anharmonic behavior near magnetic transition as it shows sudden softening of the phonon modes. This deviation is well supported by FWHM analysis which excludes the possibility of magnetostriction effect induced phonon anomaly. Whereas, renormalized phonon frequency and normalized magnetic moment model given by mean-field approximation are also incorporated in the present study. Both renormalized phonon frequency difference and normalized magnetic moment follow the same trend according to mean-field approximation which confirms that there is an interplay between phonon modes and magnetic spin. Thus, the present system PCFMO display spectrum of magnetic properties which is essential for the applications.